



HAL
open science

Influence of caudal fin rigidity on swimmer propulsion efficiency

Michel Bergmann, Angelo Iollo, Rajat Mittal

► **To cite this version:**

Michel Bergmann, Angelo Iollo, Rajat Mittal. Influence of caudal fin rigidity on swimmer propulsion efficiency. [Research Report] RR-8475, INRIA. 2014, pp.20. hal-00945912

HAL Id: hal-00945912

<https://inria.hal.science/hal-00945912>

Submitted on 13 Feb 2014

HAL is a multi-disciplinary open access archive for the deposit and dissemination of scientific research documents, whether they are published or not. The documents may come from teaching and research institutions in France or abroad, or from public or private research centers.

L'archive ouverte pluridisciplinaire **HAL**, est destinée au dépôt et à la diffusion de documents scientifiques de niveau recherche, publiés ou non, émanant des établissements d'enseignement et de recherche français ou étrangers, des laboratoires publics ou privés.



Influence of caudal fin rigidity on swimmer propulsion efficiency

Michel Bergmann, Angelo Iollo , Rajat Mittal

**RESEARCH
REPORT**

N° 8475

February 2014

Project-Teams MC2



Influence of caudal fin rigidity on swimmer propulsion efficiency

Michel Bergmann* †, Angelo Iollo* †, Rajat Mittal‡

Project-Teams MC2

Research Report n° 8475 — February 2014 — 20 pages

Abstract: A computational model is used to examine the effect of caudal fin flexibility on the propulsive efficiency of a self-propelled swimmer. The computational model couples a penalization method based Navier-Stokes solver with a simple model of flow induced deformation and self-propelled motion at an intermediate Reynolds number of about 1000. The results indicate that a significant increase in efficiency is possible by careful choice of caudal fin rigidity. The flow-physics underlying this observation is explained through the use of a simple hydrodynamic force model.

Key-words: Caretsian grid, immersed boundaries, fish-like swimming, efficiency, tail rigidity

* Inria, F-33400 Talence, France.

† Univ. Bordeaux, IMB, UMR 5251, F-33400 Talence, France

‡ Department of Mechanical Engineering, Johns Hopkins University, Baltimore, Maryland 21218, USA

**RESEARCH CENTRE
BORDEAUX – SUD-OUEST**

200 avenue de la Vieille Tour
33405 Talence Cedex

Influence de la flexibilité de la nageoire caudal sur l'efficacité de la nage

Résumé : Dans ce rapport nous nous intéressons à la modélisation et à la simulation numérique de l'efficacité de la nage d'un poisson autopropulsé. En particulier, l'influence de la flexibilité de la nageoire caudale est étudiée. L'écoulement fluide est modélisé et simulé numériquement sur un maillage cartésien à l'aide de méthodes de pénalisation et de frontières immergées. Les résultats numériques indiquent que l'efficacité peut être grandement améliorée pour certains paramètres de flexibilité. Enfin, ce phénomène peut être expliqué à l'aide d'une modèle simplifié des forces hydrodynamiques.

Mots-clés : Maillage cartésien, frontières immergées, nage de poissons, efficacité, flexibilité de la nageoire caudale

1 Introduction

Investigation of swimming hydrodynamics can on the one hand provide insights into biological evolution and physiology, and on the other, lead to new bioinspired designs of underwater vehicles. Quantitative evaluation of the mechanical and fluid dynamical characteristics of swimming in experiments is challenging Triantafyllou et al. [2000]. In particular, precise control of the kinematics and dynamics of the experimental model is difficult; harder still is the accurate measurement of forces and power of a freely swimming model. In this regard, computational modeling and simulation is well suited for such investigation. However, three-dimensional numerical simulation of swimming modes have only become viable in the last decade [Mittal et al., 2008, Shirgaonkar et al., 2009, Curet et al., 2010, Hieber and Koumoutsakos, 2008, Gazzola et al., 2011] due to the significant complexity and computational expense involved in such simulations.

The bending of biological propulsive structures is well known [McCutchen, 1970]. Here, we thus use numerical simulation to study this specific aspect of fish-like swimming: the influence of caudal fin flexibility on the swimming performance of the so called "carangiform" mode of swimming [Sfatiotakis et al., 1999]. A number of past numerical [Dong et al., 2010, Ramamurti et al., 2002] and experimental [Lauder et al., 2006, Esposito et al., 2011] studies have examined the effect of pectoral fin deformation on labriform propulsion. However, there have been few examinations that have quantified the degree of flexibility with increase in efficiency [Bose, 1995, Prempraneerach et al., 2003, Vermeiden et al., 2012, Katz and Weihs, 1978, Heathcote et al., 2008]. Esposito et al. [2011] found that there exist optimal fin flexural rigidity for maximizing thrust at fixed point, i.e., for a flapping fin that is not displacing. Thiria and Godoy-Diana [2010] have also shown that flexible wings can lead to substantial reduction in the consumed power and to an increment of the propulsive force, also for a fixed point. Marais et al. [2012] observed a thrust enhancement by a factor three for a fixed flexible pitching foil compared to the rigid case. Vanella et al. [2009] have used a simple two-link model to investigate the potential benefits of flexibility and highlighted the importance of considering non-linear resonances for enhancing aerodynamic performance. Finally, Young et al. [2009] have examined the influence of insect wing deformation on the flight efficiency thanks to both numerical and experimental studies, highlighting the role of curvature on efficiency.

Similar studies have not been undertaken for caudal-fin propulsion of a self-propelled swimmer. The vast majority of fishes and marine mammals (especially those that can swim fast) employ their caudal fin for propulsion and it is therefore expected that an analysis of this propulsion mode will yield useful insights for the design of bioinspired swimming vehicles.

It is well known that flow patterns over the body as well as in the wake significantly influence swimming performance [Fish and Lauder, 2006, Zhu et al., 2002]. These patterns are in turn influenced by the geometry of the body as well as its kinematics. A number of past studies have examined these effects of body geometry as well as prescribed body and/or fin kinematics [Mittal et al., 2008, Shirgaonkar et al., 2009, Curet et al., 2010, Hieber and Koumoutsakos, 2008, Borazjani and Sotiropoulos, 2009, Gazzola et al., 2011]. In the current study we focus on the efficiency improvement in a self-propelled "fish" obtained by a simple and local modification of the flexural rigidity of the caudal fin. We evaluate the swimming efficiency by employing a non-dimensional index that takes into account the total mechanical power acting on the fluid, the modeled fish velocity and the force exerted in the direction of locomotion [von Loebbecke et al., 2009]. We concentrate on locomotion at low Reynolds numbers so that all the relevant scales of the flow are well resolved in these three-dimensional simulations.

2 Numerical modeling

The modeling of the flow past a deformable body and the numerical method employed (§2.1) are basically the same as those described in Mittal et al. [2008] and Bergmann and Iollo [2011] and we only provide a brief description of the salient features.

2.1 Flow around deformable bodies

The flow is modeled by the incompressible Navier-Stokes equations (1). The kinematics of the deforming body are prescribed. The kinematics of the caudal fin can either be prescribed or computed from a unidirectional flow-induced deformation model. The trajectory of the modeled fish is computed from the integral force and torque exerted on the swimmer surface. The displacement of the swimmer across the domain is implemented via Lagrangian markers that are attached to the swimmer surface. The domain under consideration is a three-dimensional box $\Omega = \Omega_f \cup \Omega_s$ (the "aquarium"), where Ω_f is the domain filled by fluid, and Ω_s is the domain defined by the swimmer. The outer boundary and the swimmer surface are denoted by $\partial\Omega_f$ and $\partial\Omega_s$ respectively. Given this, the governing incompressible Navier-Stokes equations are given by:

$$\rho \left(\frac{\partial \mathbf{u}}{\partial t} + \rho(\mathbf{u} \cdot \nabla) \mathbf{u} \right) = -\nabla p + \mu \Delta \mathbf{u} \text{ in } \Omega_f, \quad (1a)$$

$$\nabla \cdot \mathbf{u} = 0 \text{ in } \Omega_f, \quad (1b)$$

with initial conditions $\mathbf{u}(\mathbf{x}, 0) = \mathbf{u}_0(\mathbf{x})$ in Ω_f , boundary conditions $\mathbf{u}(\mathbf{x}, t) = \mathbf{0}$ on $\partial\Omega_f$ and $\mathbf{u}(\mathbf{x}, t) = \mathbf{u}_s(\mathbf{x}, t)$ on $\partial\Omega_s$. Equations (1) are discretized in time with a second-order projection scheme [Chorin, 1968] and spatially discretized on a fixed Cartesian mesh with grid spacing of $\Delta x = \Delta y = \Delta z = h$. Since the swimmer boundary $\partial\Omega_s$ is curvilinear the Cartesian mesh does not conform to this boundary; the boundary conditions $\mathbf{u}(\mathbf{x}, t) = \mathbf{u}_s(\mathbf{x}, t)$ on $\partial\Omega_s$ are therefore imposed using a discrete forcing immersed boundary method and penalization [Mittal and Iaccarino, 2005, Mittal et al., 2008, Bergmann and Iollo, 2011].

2.2 Modeled fish geometry and deformation

We consider a prototype swimmer of unit length, $\ell = 1 m$. At rest, the midline (backbone) of the fish-like geometry coincides with $0 \leq x \leq 1, y = z = 0$. This backbone is then discretized by "vertebra" located at x_i for $i = 1, \dots, N$. The three-dimensional fish-like shape is reconstructed using N ellipses with minor-axes $y(x_i)$ and $z(x_i)$. These axes lengths are found using B-splines (see figure 1). The maximum transverse dimensions are $2y = 0.17$ and $2z = 0.24$ and the caudal fin has a maximal vertical span $2z = 0.25$. These values are chosen to approximately mimic the MIT robot bluefin tuna [Barrett et al., 1999]. The final swimmer geometry is presented in figure 1.

The shape of the swimming body is obtained by deforming the body midline in the plane $z = 0$ as a function of time while keeping each elliptic cross-section to be orthogonal to the midline during deformation. The body surface is discretized as $\partial\Omega_s = \cup_{i=1}^{N_s} \partial\Omega_s^i$, where N_s denotes the number of surface sections and $\partial\Omega_s^i$ defines a covering space of the surface. The velocity of each surface element, noted $\mathbf{u}_s(\mathbf{x}_i, t)$, is then computed by tracking the Lagrangian markers corresponding to each surface element for $i = 1, \dots, N_s$.

Based on previous work, the deformation of the midline is based on a traveling wave with a space-dependent amplitude [Barrett et al., 1999, Bergmann and Iollo, 2011] as

$$y_{mid}(x) = a(x) \sin(kx - \omega t), \quad (2)$$

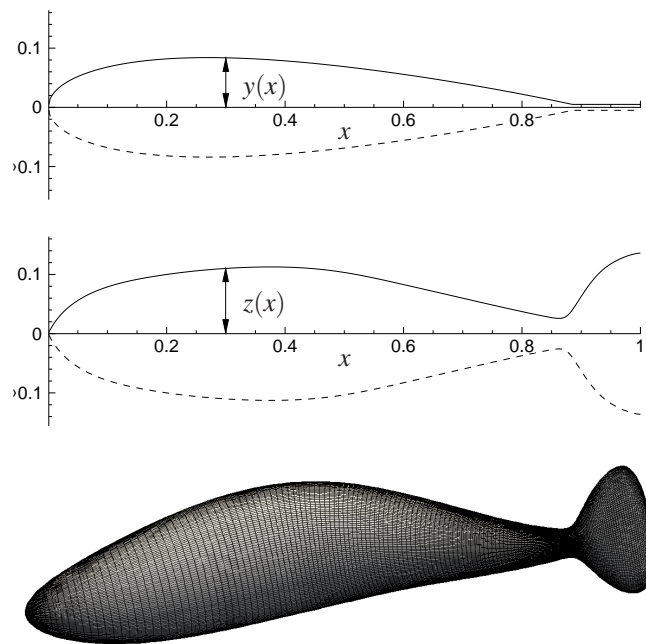


Figure 1: Representation of the elliptical axes $y(x)$ and $z(x)$ defining the fish shape.

where $k = 2\pi/\lambda$ denotes the wave number associated with a wavelength λ and $\omega = 2\pi f$ denotes the pulsation of the oscillations associated with frequency f . The amplitude envelope $a(x) = c_0 + c_1x + c_2x^2$ is usually defined by three parameters c_0 , c_1 and c_2 that can be adjusted. There is one constraint (the back bone length) and 4 independent parameters: c_0 , c_1 , c_2 and the abscissa of the tail extremity. Therefore we have the possibility of choosing 3 of these parameters and to determine the last thanks to the constraint. We reach a desired maximal tail excursion denoted by A , while the backbone length remains $\ell = 1 m$. In what follows we will take $c_0 = c_2 = 0$ and $c_1 = 0.1$. These values correspond to a linear growth of the backward traveling wave and result in a swimming law that qualitatively agrees with those observed in *Trachurus*. However, these are not the values necessarily observed in a specific actual fish swimming.

Without action of external forces the center-of-mass of the swimmer should not move. To respect this constraint, after deforming the swimmer as explained above, we subtract the motion of the center-of-mass from the displacement of each Lagrangian marker on the fish surface.

2.3 Caudal fin modeling

The primary objective here is to assess the effect of caudal fin flexibility on swimming performance. To this end, the deformation can be either imposed on the whole midline length including the caudal fin (black shape shown in figure 2), or only on the portion excluding the caudal fin (which extends over the last 20% of the midline, see red or blue shapes in figure 2). For these latter cases, we model the fin by a lumped parameter elastic medium. The elastic caudal tail is composed by rigid struts joined by elastic links. Each link is subject to a couple C_i that is proportional to the square of the local tangential speed V_{i+1} of the next junction. This couple is a crude approximation of the hydrodynamic local force exerted by the fluid on the structure. In section 4 we will show that this hypothesis is approximatively verified in our simulations.

To further simplify the model, we assume that the angles are small and the inertia and hydrodynamic forces balance for the struts following the one considered. Then, we have

$$\ddot{\theta}_i + \beta \dot{\theta}_i + k\theta_i = C_i, \quad i = 1, \dots, N_L - 1$$

where θ_i is the rotation angle with respect to the previous strut, $C_i = -\alpha|V_{i+1}|V_{i+1}$, N_L is the number of links, $V_i = il \sum_{k=1}^i \dot{\theta}_k$, l is the length of the struts. The point $i = 0$ corresponds to 0.8 of the midline and is the last point where the deformation is explicitly imposed by (2). This equation corresponds to a classical spring-damper system with a forcing term that couples the system. The angular acceleration of a strut with respect to the previous is proportional to the sum of the couple exerted on the strut, the elastic force and the damping force. The initial condition is $\theta_i = 0, \forall i$. In the following examples we let $\beta = 1, k = 4 \cdot 10^3, 0 \leq \alpha \leq 16 \cdot 10^{-2}$ and $N_L = 60$. These parameters were selected to obtain a realistic deformation of the tail, as in figure 2.

In summary, this crude model keeps the essential features of a visco-elastic structure, such as elastic recoil and velocity damping, mimicking the feed-back effects of actual fluid forces via the terms C_i .

2.4 Force, torque and power

Let the dimensionless stress tensor $\mathbb{T}(\mathbf{u}, p) = -p\mathbf{I} + \frac{1}{Re}(\nabla\mathbf{u} + \nabla\mathbf{u}^T)$ and \mathbf{n} the unit outward vector to $\partial\Omega_s$, then the forces and the torques exerted by the fluid onto the bodies are:

$$\mathbf{F}_s = - \int_{\partial\Omega_s} \mathbb{T}(\mathbf{u}, p) \mathbf{n} \, d\mathbf{x}, \quad \mathbf{M}_s = - \int_{\partial\Omega_s} \mathbf{r}_G \wedge (\mathbb{T}(\mathbf{u}, p) \mathbf{n}) \, d\mathbf{x}, \quad (3)$$

with $\mathbf{r}_G = \mathbf{x} - \mathbf{x}_G$ (\mathbf{x}_G center of mass). Since the boundary $\partial\Omega_s$ does not fit the computational mesh that will be employed, \mathbf{u} and p are obtained using Lagrange interpolation. These forces and torques are used to compute the swimmer displacement. The velocity at the swimmer surface is:

$$\mathbf{u}_s = \bar{\mathbf{u}} + \hat{\mathbf{u}} + \tilde{\mathbf{u}}. \quad (4)$$

where $\tilde{\mathbf{u}}$ is the imposed deformation velocity, $\bar{\mathbf{u}}$ is the translation velocity and $\hat{\mathbf{u}}$ is the rigid rotation velocity. The translation velocity can be computed from the forces \mathbf{F}_s by $m \frac{d\bar{\mathbf{u}}}{dt} = \mathbf{F}_s$, m being the body mass. The rotation velocity is given by $\hat{\mathbf{u}}_s = \Theta_s \times \mathbf{r}_G$. The angular velocity Θ_s is obtained from the torques \mathbf{M}_s by solving $\frac{dJ\Theta_s}{dt} = \mathbf{M}_s$, where J denoted the body inertia matrix.

The force exerted by the fluid on the body surface segment $\partial\Omega_s^i$ is

$$\mathbf{F}^i = (F_x^i, F_y^i, F_z^i)^T = - \int_{\partial\Omega_s^i} \mathbb{T}(\mathbf{u}, p) \cdot \mathbf{n} \, d\mathbf{x},$$

where \mathbf{n} the unit outward vector to $\partial\Omega_s^i$. The total work done over one stroke T is then:

$$W_{total} = \int_T \sum_{i=1}^{N_s} \mathbf{F}^i \cdot \mathbf{u}^i \, dt, \quad (5)$$

where \mathbf{u}^i is the average velocity on the surface $\partial\Omega_s^i$. The useful work is defined as the part of the total work that is done by the hydrodynamic force exerted in the direction of swimming [von Loebbecke et al., 2009]. For instance, if the swimmer velocity is positive in the x -direction, $U_x > 0$, then the useful work is given by:

$$W_{useful} = \int_T \sum_{i=1}^{N_s} \frac{F_x^i + |F_x^i|}{2} U_x^i \, dt. \quad (6)$$

The propulsive efficiency can then be defined as

$$\eta = \frac{W_{useful}}{W_{total}}.$$

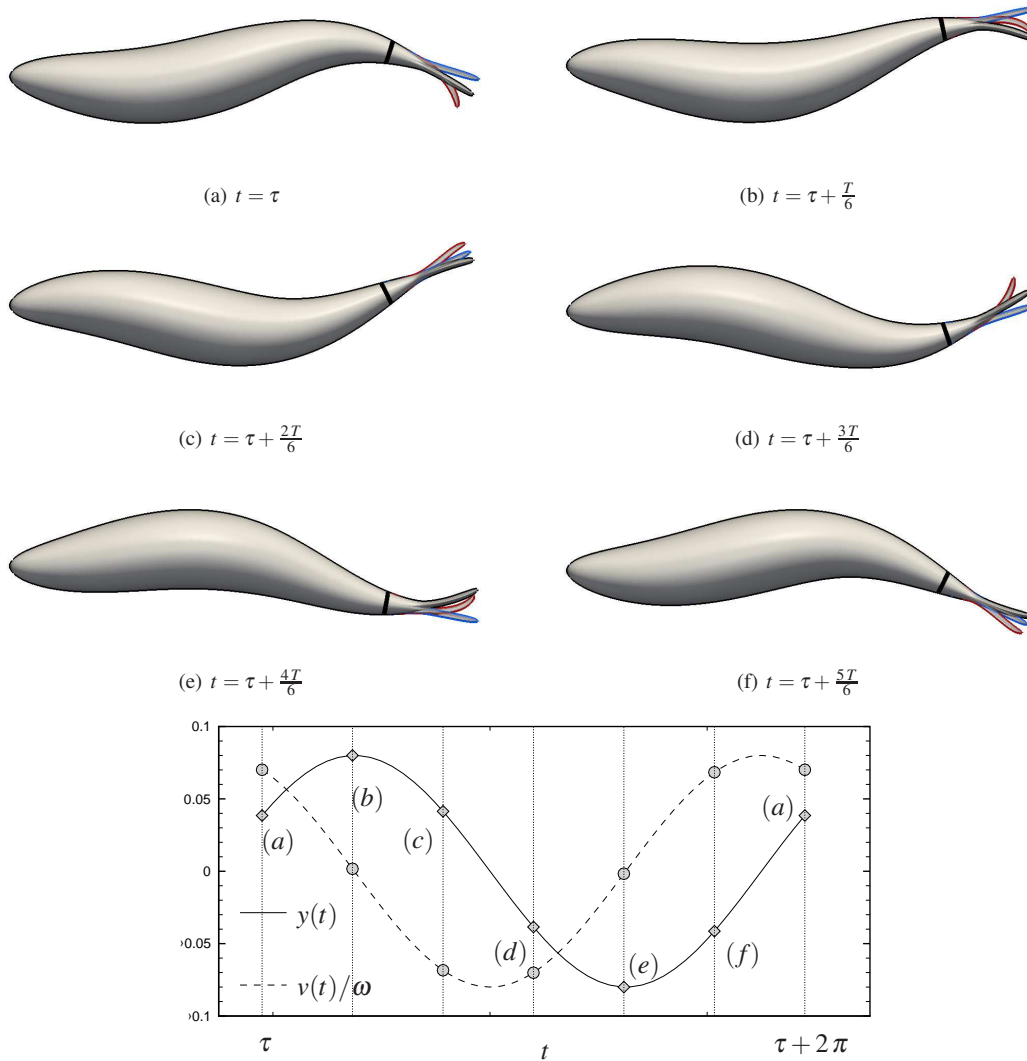


Figure 2: Deformation of the swimmer over one swimming stroke T (corresponding to a frequency $f = 2.0Hz$). The same sinusoidal swimming law is applied on the whole shape except between the black section and the tail extremity where an elastic behavior can be used. The black shape corresponds to an imposed tail deformation, the blue shape corresponds to a rigid tail and the red shape corresponds to a flexible tail.

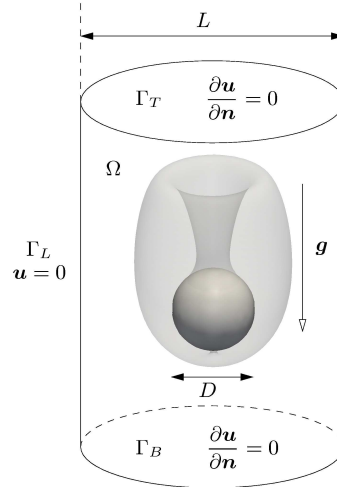


Figure 3: Sketch of a sphere sedimentation, with an example of iso-vorticity representation.

3 Numerical validations

The numerical method employed has been extensively validated for several 2D test cases in Bergmann and Iollo [2011]. In what follows, 3D validations are presented. We first study the terminal velocity of a sphere falling under gravity. Then we perform a convergence study of the terminal velocity of a swimming fish with respect to spatial discretization. Finally, we show that the assumption $C_i = -\alpha|V_{i+1}|V_{i+1}$ is reasonably verified for swimming laws similar to those investigated later in this paper.

3.1 Sedimentation of a sphere

Both experimental [Clift et al., 1978] and numerical [Glowinski et al., 2001, Coquerelle and Cottet, 2008] results are found in the literature for the sedimentation of a sphere under the gravity. The sketch of the configuration is given in figure 3. We chose the same non-dimensional parameters as Coquerelle and Cottet [2008], the sphere (diameter D) falls under gravity in an vertical cylinder (diameter $L = 1$) filled with a fluid of viscosity ν under the gravity $g = -980$. We model an infinite cylinder and impose homogeneous Neumann boundary conditions ($\frac{\partial \mathbf{u}}{\partial \mathbf{n}} = \mathbf{0}$ where \mathbf{n} is the outward normal unit vector) at the top and bottom boundaries, respectively Γ_T and Γ_B . No slip boundary conditions, $\mathbf{u} = \mathbf{0}$, are imposed on the cylinder lateral boundary, Γ_L , using penalization [Angot et al., 1999]. Table 1 presents a comparison between terminal velocities for various diameters and viscosities. The terminal velocity, U , computed in this study is compared with experimental results U_E obtained by Clift et al. [1978] and numerical results U_G and U_C obtained by Glowinski et al. [2001] and Coquerelle and Cottet [2008] respectively. The results reported in table 1 are computed with a spatial discretization $h = 1/100$. Our results are comparable to those in the literature. These are typical results for several computational set up parameters.

3.2 Swimming velocity convergence

We perform a convergence study for a unitary length swimmer with respect to the grid size. The kinematic viscosity is set to $10^{-3} m^2 s^{-1}$. The two quantities under consideration are the forward velocity $\langle V \rangle$ and the efficiency $\langle \eta \rangle$ ($\langle \cdot \rangle$ denotes an averaging operator acting on a given number of periods when

D	ν	U_E	U_G	U_C	U
0.2	0.10	0.2571	0.2567	0.256	0.266
0.2	0.05	0.4603	0.4844	0.475	0.497
0.2	0.02	0.9129	0.9480	0.937	0.953
0.3	0.10	0.4047	0.4072	0.401	0.420
0.3	0.05	0.7493	0.7599	0.748	0.764
0.3	0.02	1.4359	1.3920	1.390	1.472

Table 1: Comparison between terminal velocities for spheres falling in a fluid for various diameters and viscosities.

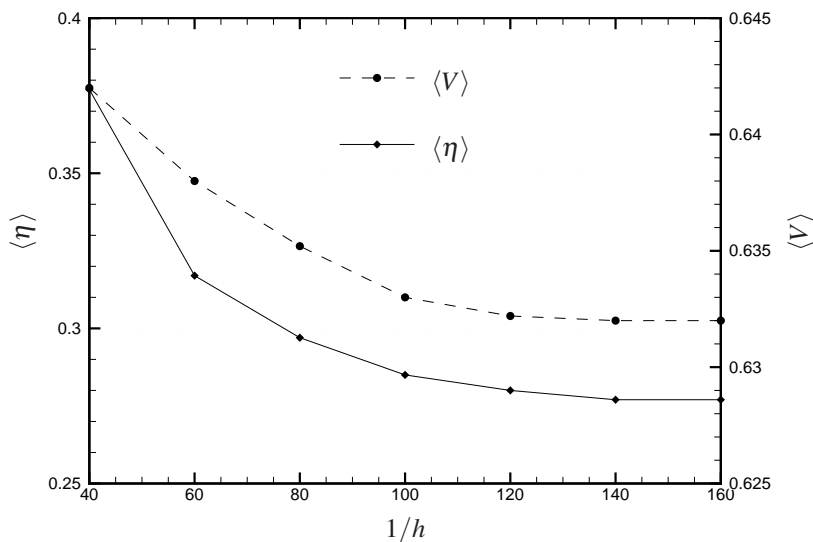


Figure 4: Convergence study of the swimmer velocity $\langle V \rangle$ the efficiency $\langle \eta \rangle$ versus the grid size $(1/h)$. The brackets denote an averaging operator.

asymptotic velocity is reached). Figure 4 shows the evolutions of the swimmer velocity norm and efficiency (averaging on the last stroke period) versus the grid size $1/h$ (here, we have $h = \Delta x = \Delta y = \Delta z$). Both velocity and efficiency tend to converge towards limit values for fine meshes. Obviously, accuracy is improved with mesh size. However, the case $h = 1/120$ is a good compromise between accuracy and computation costs. Indeed, the errors between $h = 1/120$ and $h = 1/160$ are about 2% and $h = 1/120$ requires half CPU time than $h = 1/160$. We then set our spatial resolution to $h = 1/120$ for the following simulations. The domain under consideration is $x \in [-2, 6]$, $y \in [-2, 2]$ and $z \in [-2, 2]$. The finest mesh is then composed by $8 \times 4 \times 4 \times 160^3 \approx 5 \cdot 10^8$ mesh nodes. We considered the physical domain as an aquarium and imposed thus homogeneous boundary condition on all boundaries. In all the following simulations we used the same domain $x \in [-2, 6]$, $y \in [-2, 2]$ and $z \in [-2, 2]$ with $h = 1/120$ and the mesh is composed by $8 \times 4 \times 4 \times 120^3 \approx 2.2 \cdot 10^8$ mesh nodes.

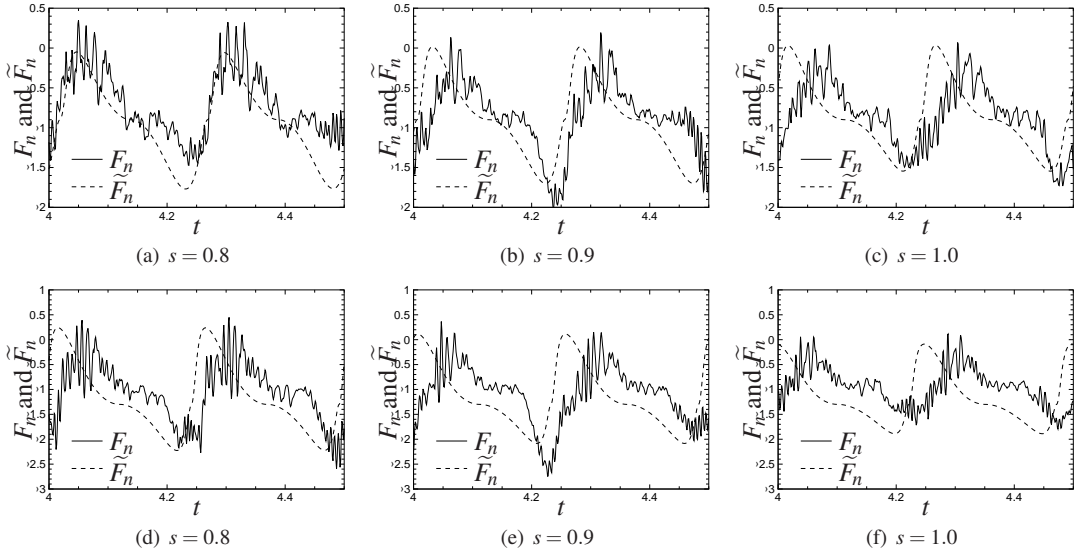


Figure 5: Force F_n on a tail section at abscissa s compared to $\tilde{F}_n = \gamma|V_n|V_n$, where V_n is the normal speed of the swimmer centerline (the backbone). The parameter γ is adjusted to scale \tilde{F}_n with F_n .

3.3 Force on caudal fin section

In the one-way elastic model that we have set up the force acting on the struts as $\tilde{F}_n = \gamma|V_n|V_n$, where V_n is the normal speed of the swimmer centerline (the backbone). We compare the actual force obtained for a self-propelling swimmer on a given section to \tilde{F}_n . The computational set up corresponds identically to that of maximum efficiency of the next section. Three different sections are considered and the results are presented in figure 5. The top picture row shows the actual force computed on the given section vs. the model force \tilde{F}_n on the same section. The model force is smoother but it is in substantial agreement with the actual force. The phase error is limited. The bottom picture row shows the same comparison for a model force \tilde{F}_n computed considering the normal velocity of a section that is $\Delta s = 0.05$ upstream. The overall deformation of the backbone will be modified and the swimming law will consequently vary. The phase error between the actual force experienced by each section considered and \tilde{F}_n increases, confirming the hypothesis the normal force locally scales like $|V_n|V_n$. We conclude that the simplified force model is a reasonable approximation of the actual force experienced by the swimmer. With this model the fluid-structure interaction is one way and this significantly simplifies the computational set up.

4 Efficiency

We set the kinematic viscosity $\nu = 10^{-3} m^2 s^{-1}$. The swimmer is of unitary length $\ell = 1 m$ and hence the swimming Reynolds number is $1000V$, where V the swimming velocity. Such low Reynolds numbers are chosen so as to enable high resolution of the flow. We note that a swimmer swimming at a velocity of around one body-length per time unit, $Re = 10^3$ can be correlated to a small swimmer of $3 cm$ long.

4.1 Tail rigidity

We have considered a large range of the rigidity parameter α : from 0.02 (low-flexibility tail) to 0.16 (high-flexibility tail). These parameters are not directly related to the elasticity modulus of a given material, rather they are relative to the simplified elasticity model we employ. The variation of the efficiency versus the rigidity parameter α for $f = 2$ is shown in figure 6(a). We found that a value of $\alpha = 0.1$ maximize the efficiency and that the flexible tail increases the efficiency by about 25% in comparison to the case where the deformation is prescribed for the whole body. Figure 8 shows a snapshot of the vorticity field generated by the swimmer with maximum efficiency ($\alpha = 0.1$); the swimmer generates a vortex street composed of two oblique rows of vortex rings, similar to that generated by a flapping foil [Dong et al., 2006]. This is characteristic of the wake generated for higher values of the swimming Strouhal number $St = \frac{fA}{V}$ [Dai et al., 2012], typically for $St \geq 0.3$ [Borzajani and Sotiropoulos, 2009]. Here, the minimum swimming Strouhal number obtained for the swimming law considered is approximately 0.5.

In previous comparisons the swimmer velocity V was allowed to vary with α which introduced potentially confounding effects in the Reynolds numbers. In order to eliminate these effects, we have investigated the variation of the efficiency for a constant swimming velocity. In these cases, the frequency is kept at $f = 2.0$ and the tail amplitude A is regulated by a proportional feed-back controller to reach a target velocity of $V = 0.4 m.s^{-1}$, which is the minimum velocity obtained for $\alpha = 0.16$. It happens that the tail excursion A is approximately constant for all α s leading to a similar swimming Strouhal number St . Figure 7(a) presents the evolution of the efficiency versus α and we find that that $\alpha \geq 0.04$ produces a higher efficiency compared to the rigid tail. In fact, for $\alpha = 0.12$ the efficiency is increased by 35%. This quite high increase for $\alpha = 0.12$ can be explained by the increase of the useful work and the decrease of the total work over one stroke (see figure 7(b)).

4.2 Influence of tail curvature

In this section we investigate the influence of tail curvature on the swimming efficiency. We do that by varying the number of links in the tail. In the previous simulation we employed $N_L = 60$ links on the tail. In what follows, we take $1 \leq N_L \leq 5$ as presented in figure 9. The case $N_L = 60$ corresponds to $\alpha = 0.12$. and the parameter α is modified for $1 \leq N_L \leq 5$ so that the trajectory of the tail is as close as possible to the one for $N_L = 60$ with $\alpha = 0.12$. Note that the shape for $N_L = 5$ is similar to that with $N_L = 60$. Figure 10(a) shows that efficiency is enhanced when curvature is increased (N_L is increased). The evolution of the useful and total work versus the number of links N_L in presented in figure 10(b). While the value of the useful work is almost constant with N_L , the total work done by the swimmer over one stroke decreases with increasing N_L and eventually reaches the value obtained for our test case with $N_L = 60$. An optimal value of the flexural rigidity help to decrease the work done by the swimmer, especially the contribution due to the lateral motion. Indeed, when the swimmer velocity is constant, the total work is equal to the work done by the lateral motion.

5 A simple model for tail design

The largest forces and velocities on the swimmer are located on the tail. Let us consider the local contribution of the useful work $\overline{W}_{useful}(x)$ relative to each section normal to the midline at abscissa x . We define by $W_x = 100 \frac{\overline{W}_{useful}(x)}{W_{useful}}$ the percentage of the useful work generated between abscissa x and 1. In figure 11 we see that 75% of the total useful work is contributed by the caudal fin, i.e., the last 12% of the swimmer. Hence, in order to obtain a simple interpretation of flow physics underlying our observations of efficiency enhancement, we now focus only on the tail segment, denoted by κ . Let \mathbf{e}_θ be the normal to κ as in figure 12. The relative velocity of the mid point of κ with respect to swimmer velocity is denoted

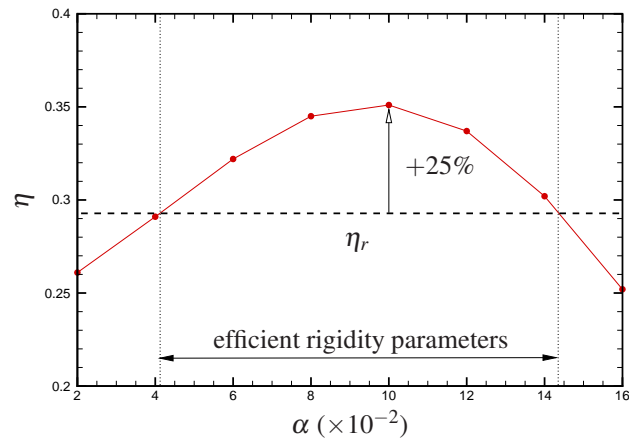
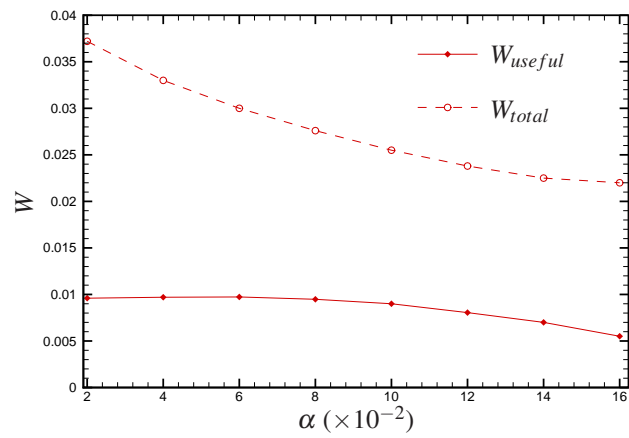
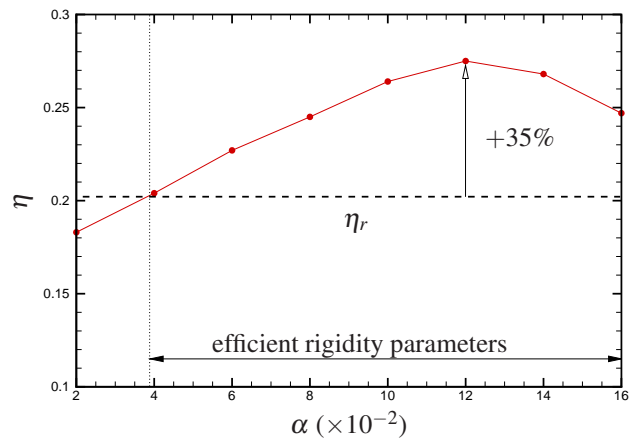
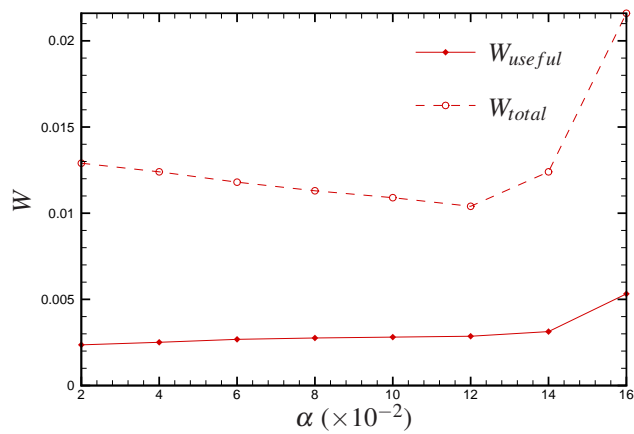
(a) η vs. α (b) W_{useful} and W_{total} vs. α

Figure 6: Evolution of the efficiency η , the useful work W_{useful} and the total work W_{total} versus the rigidity parameter α . The dotted line corresponds to the imposed tail deformation.



(a) η vs. α for $V = 0.4m.s^{-1}$



(b) W_{useful} and W_{total} vs. α for $V = 0.4m.s^{-1}$

Figure 7: Evolution of the efficiency η , the useful work W_{useful} and the total work W_{total} versus the rigidity parameter α for $V = 0.4m.s^{-1}$. The dotted line correspond to imposed tail deformation for $V = 0.4m.s^{-1}$

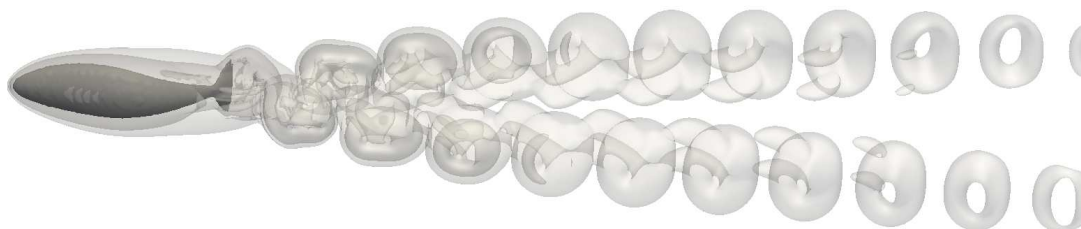


Figure 8: Vorticity snapshot of the wake generated by the modeled swimmer with $\alpha = 0.1$ at $Re = 10^3$.

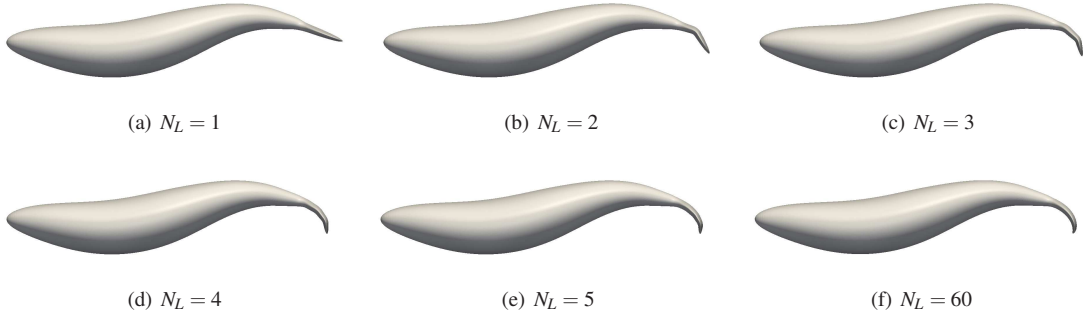


Figure 9: Swimmer shapes for different values of the number of links (N_L). The case $N_L = 60$ correspond to $\alpha = 0.12$.

by $\mathbf{v} = (v_x, v_y)$ and let the force exerted by κ on the fluid be \mathbf{F} . The normal component of this force is mainly generated by the pressure jump, whereas the tangential force is generated by viscous effects. As a first approximation, we neglect the viscous contributions since the Reynolds number is relatively high. In this limit, we model the force by $\tilde{\mathbf{F}} = (f_x, f_y) = \beta(\mathbf{e}_\theta \cdot \mathbf{v})|\mathbf{v}|\mathbf{e}_\theta$, where $\beta > 0$ is a real constant. Thrust is generated when $f_x > 0$. The useful work is then $\tilde{W}_{useful} = \int_T \frac{f_x + |f_x|}{2} v_x dt$, the work generated by lateral motion is $\int_T f_y v_y dt$ and the total work is $\tilde{W}_{total} = \int_T \tilde{\mathbf{F}} \cdot \mathbf{v} dt$. The efficiency resulting from this model is then $\tilde{\eta} = \frac{\tilde{W}_{useful}}{\tilde{W}_{total}}$.

Figure 13(b) shows the evolution of \tilde{W}_{useful} and \tilde{W}_{total} versus α . We scaled β as $\beta = 0.06$ so that the useful and total work are in the same ranges as in figure 6(b). The tendencies are similar to those obtained in figure 13(b), except for the largest values of α . The plot of $\tilde{\eta}$ versus α is presented in figure 13(a). Even if the values of $\tilde{\eta}$ are slightly different from that of η obtained in figure 6(a), the overall trends are found to be similar. Indeed, the maximum efficiency is obtained for the same value of α ($=0.12$) in both cases.

In figure 14 we show the trajectory of κ and the corresponding model forces as a function of the tail rigidity. For rigid tails ($\alpha = 0.02$) the forces are propulsive over the whole cycle but they are small in intensity and have large vertical components. For optimal rigidity ($\alpha = 0.10$) the forces are propulsive over most of the cycle; their modulus is comparatively large and the vertical components are small. For high flexibility ($\alpha = 0.16$) the vertical forces are small but the horizontal force is drag-generating over nearly half of the cycle. For this last case, the integral contribution over one period of the forces in the x direction becomes negative.

6 Conclusions

The effect of tail flexibility on swimming performance has been examined via Navier-Stokes simulations coupled with a lumped-element model of the flexible caudal fin. Our results show that allowing caudal fin deformation induced by a simple elastic model has a marked influence on the propulsive performance of the swimmer. The model shows that optimal efficiency is obtained for an intermediate flexibility of the caudal fin and that neither excessive rigidity nor compliance are conducive to efficient propulsion. We further show that a limited number of links (≈ 3) in the tail is able to generate tail curvatures sufficient to reach efficiencies obtained with a larger number of links. Our investigation is valid for low Reynolds number regimes and without taking into account possible skin effects (like polymer release) or small-scale compliant-tissue effects. Furthermore, an interpretation of these results is given based on a purely

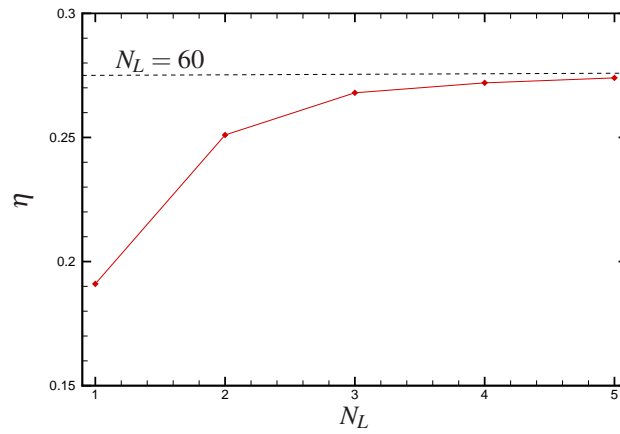
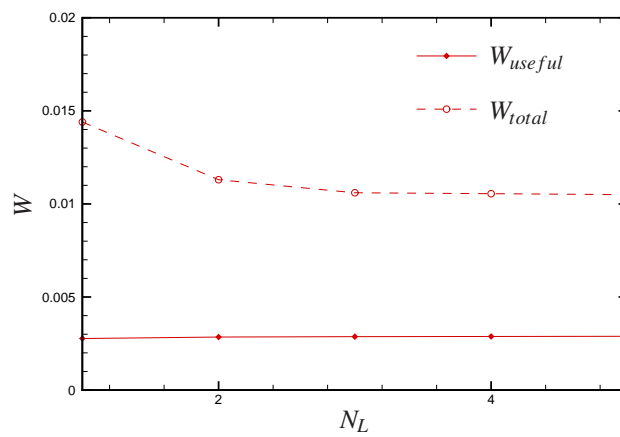
(a) η vs. N_L for $V = 0.4m.s^{-1}$ (b) W_{useful} and W_{total} vs. N_L for $V = 0.4m.s^{-1}$

Figure 10: Evolution of the efficiency η , the useful work W_{useful} and the total work W_{total} versus the number of links N_L for $V = 0.4m.s^{-1}$. The dotted line corresponds to imposed tail deformation for $V = 0.4m.s^{-1}$

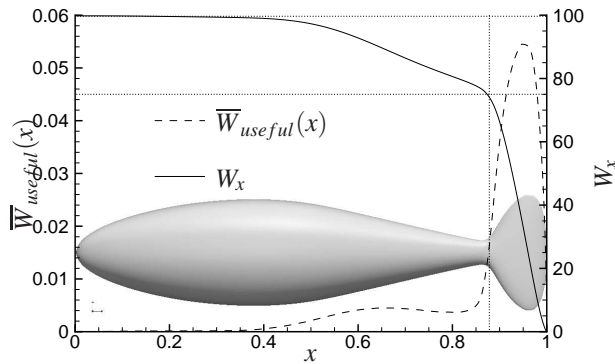


Figure 11: Evolution of the local useful work contribution along the midline and overall useful work generated starting from the caudal fin.

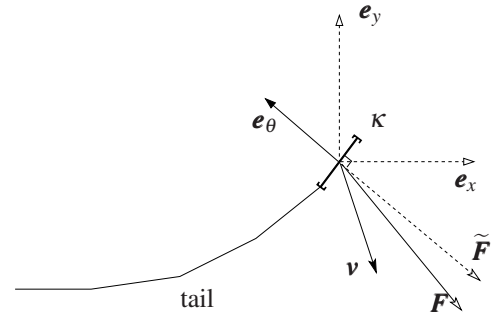


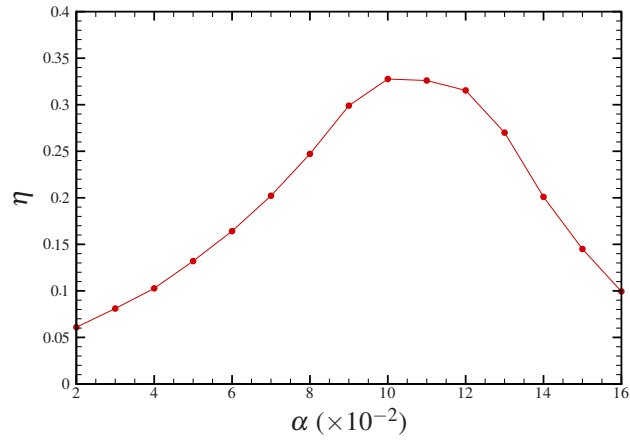
Figure 12: Sketch of the tail in the simplified efficiency model.

kinematic model. We observe that rigid caudal fins lead to excessive lateral forces that increase power consumption without generating thrust, whereas highly flexible caudal fins produces negative thrust during significant portions of the stroke. These results may lead to significant improvements in the design of underwater robots and suggest bioinspired designs for flexible fin propulsors.

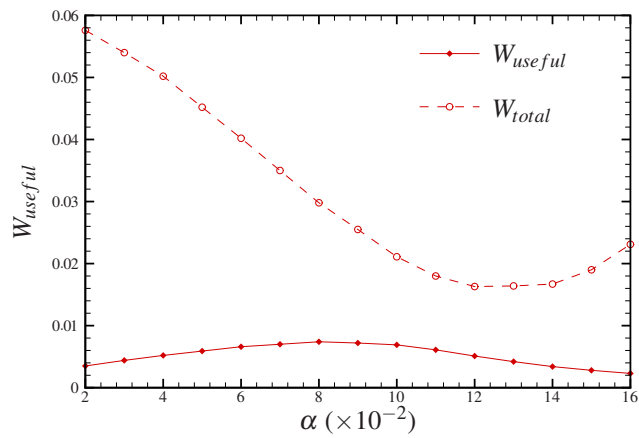
This work has been supported by French National Research Agency (ANR) through COSINUS program (project CARPEINTER n. ANR-08-COSI-002). The simulations presented in this paper were carried out using the PLAFRIM experimental parallel testbed, being developed under the Inria PlaFRIM development action with support from LABRI and IMB and other entities: Conseil Régional d'Aquitaine, FeDER, Université de Bordeaux and CNRS (see <https://plafirim.bordeaux.inria.fr/>).

References

- P. Angot, C.H. Bruneau, and P. Fabrie. A penalization method to take into account obstacles in a incompressible flow. *Num. Math.*, 81(4):497–520, 1999.
- D.S. Barrett, M.S. Triantafyllou, D.K.P. Yue, M.A. Grosenbauch, and M.J. Wolfgang. Drag reduction in fish-like locomotion. *J. Fluid Mech.*, 392:182–212, 1999.
- M. Bergmann and A. Iollo. Modeling and simulation of fish-like swimming. *Journal of Computational Physics*, 230(2):329 – 348, 2011. ISSN 0021-9991.
- Iman Borazjani and Fotis Sotiropoulos. Why don't mackerels swim like eels? The role of form and kinematics on the hydrodynamics of undulatory swimming. *Physics of Fluids*, 21(9):091109, 2009.
- N. Bose. *Performance of chordwise flexible oscillating propulsors using a time-domain panel method*, volume 42. International shipbuilding progress, 1995.
- A.J. Chorin. Numerical solution of the Navier-Stokes equations. *Math. Comp.*, 22:745–762, 1968.
- R. Clift, J. R. Grace, and M. E. Weber. *Bubbles, Drops, and Particles*. Academic Press, New York, 1978.



(a) η vs. α



(b) W_{useful} and W_{total} vs. α

Figure 13: Evolution of the efficiency $\tilde{\eta}$, the useful work \tilde{W}_{useful} and the total work \tilde{W}_{total} versus the rigidity parameter α . The dotted line corresponds to the imposed tail deformation.

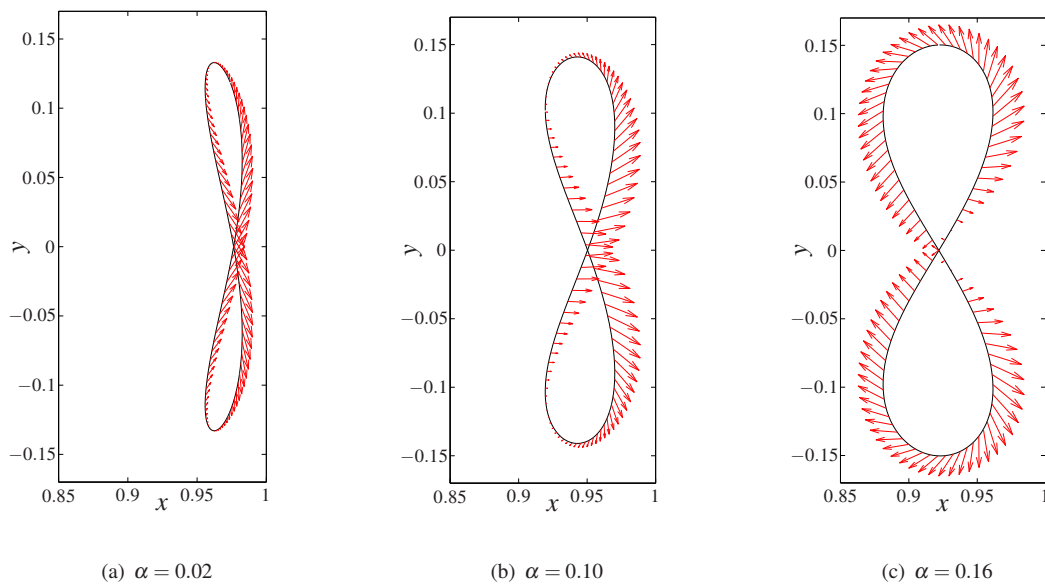


Figure 14: Trajectory of κ mid-point and corresponding force $\tilde{\mathbf{F}}$ for different values of α .

M. Coquerelle and G.H. Cottet. A vortex level set method for the two way coupling of an incompressible fluid with colliding rigid bodies. *J. Comput. Phys.*, 227(21):9121–9137, 2008.

Oscar M. Curet, Ibrahim K. AlAli, Malcolm A. MacIver, and Neelesh A. Patankar. A versatile implicit iterative approach for fully resolved simulation of self-propulsion. *Computer Methods in Applied Mechanics and Engineering*, 199:2417 – 2424, 2010. ISSN 0045-7825.

Hu Dai, Haoxiang Luo, Paulo J S A Ferreira de Sousa, and James F Doyle. Thrust performance of a flexible low-aspect-ratio pitching plate. *Physics of Fluids*, 24(10):101903, 2012.

H Dong, R Mittal, and F M Najjar. Wake topology and hydrodynamic performance of low-aspect-ratio flapping foils. *Journal of Fluid Mechanics*, 566:309, October 2006.

H. Dong, M. Bozkurtas, R. Mittal, P. Madden, and G.V. Lauder. Computational modeling and analysis of the hydrodynamics of a highly deformable fish pectoral fin. *Journal of Fluid Mechanics*, 645:345–373, 2010.

C J Esposito, J L Tangorra, B E Flammang, and G V LAUDER. A robotic fish caudal fin: effects of stiffness and motor program on locomotor performance. *Journal of Experimental Biology*, 215(1): 56–67, December 2011.

F.E. Fish and G.V Lauder. Passive and active flow control by swimming fishes and mammals. *Annu. Rev. Fluid Mech.*, 38:193–224, 2006.

Mattia Gazzola, Philippe Chatelain, Wim M. van Rees, and Petros Koumoutsakos. Simulations of single and multiple swimmers with non-divergence free deforming geometries. *Journal of Computational Physics*, 230(19):7093 – 7114, 2011. ISSN 0021-9991.

- R. Glowinski, T.-W. Pan, T.I. Hesla, D.D. Joseph, and J. Périaux. A fictitious domain approach for the direct simulation of incompressible fluid flow past moving rigid bodies: Application to particulate flow. *J. Comp. Phys.*, 169:363–426, 2001.
- Sam Heathcote, Z Wang, and Ismet Gursul. Effect of spanwise flexibility on flapping wing propulsion. *Journal of Fluids and Structures*, 24(2):183–199, 2008.
- S.E. Hieber and P. Koumoutsakos. An immersed boundary method for smoothed particle hydrodynamics of self-propelled swimmers. *Journal of Computational Physics*, 227(19):8636 – 8654, 2008. ISSN 0021-9991.
- J. Katz and D. Weihs. Hydrodynamic propulsion by large amplitude oscillation of an airfoil with chordwise flexibility. *Journal of Fluid Mechanics*, 88:485–497, 10 1978. ISSN 1469-7645.
- George V Lauder, Peter G A Madden, Rajat Mittal, Haibo Dong, and Meliha Bozkurttas. Locomotion with flexible propulsors: I. Experimental analysis of pectoral fin swimming in sunfish. *Bioinspiration & Biomimetics*, 1(4):S25–S34, December 2006.
- C. Marais, B. Thiria, J. E. Wesfreid, and R. Godoy-Diana. Stabilizing effect of flexibility in the wake of a flapping foil. *Journal of Fluid Mechanics*, 710:659–669, 2012.
- C.W. McCutchen. The trout tail fin: A self-cambering hydrofoil. *Journal of Biomechanics*, 3(3):271 – 281, 1970.
- R. Mittal and G. Iaccarino. Immersed boundary methods. *Annu. Rev. Fluid Mech.*, 37:239–261, 2005.
- R. Mittal, H. Dong, M. Bozkurttas, F.M. Najjar, A. Vargas, and A. von Loebbecke. A versatile sharp interface immersed boundary method for incompressible flows with complex boundaries. *Journal of Computational Physics*, 227(10):4825 – 4852, 2008. ISSN 0021-9991.
- P. Prempraneerach, F.S. Hover, and M.S. Triantafyllou. The effect of chordwise flexibility on the thrust and efficiency of a flapping foil. *13th Intern. Symp. Unmanned Untethered Submersible Technology*, August 24-27 2003. Durham, NH.
- R Ramamurti, W C Sandberg, R Löhner, J A Walker, and M W Westneat. Fluid dynamics of flapping aquatic flight in the bird wrasse: three-dimensional unsteady computations with fin deformation. *Journal of Experimental Biology*, 205(19):2997–3008, 2002.
- M. Sfatiotakis, D.M. Lane, and Bruce D.J. Review of fish swimming modes for aquatic locomotion. *IEEE J. Oceanic Eng.*, 24(2):237–252, 1999.
- Anup A. Shirgaonkar, Malcolm A. MacIver, and Neelesh A. Patankar. A new mathematical formulation and fast algorithm for fully resolved simulation of self-propulsion. *Journal of Computational Physics*, 228(7):2366 – 2390, 2009. ISSN 0021-9991.
- Benjamin Thiria and Ramiro Godoy-Diana. How wing compliance drives the efficiency of self-propelled flapping flyers. *Physical Review E*, 82(1):015303, 2010.
- M.S. Triantafyllou, G.S. Triantafyllou, and D.K.P Yue. Hydrodynamics of fishlike swimming. *Annual Review of Fluid Mechanics*, 32:33–53, 2000.
- Marcos Vanella, Timothy Fitzgerald, Sergio Preidikman, Elias Balaras, and Balakumar Balachandran. Influence of flexibility on the aerodynamic performance of a hovering wing. *Journal of Experimental Biology*, 212(1):95–105, 2009.

- J.G. Vermeiden, K. Kooiker, F.H. Lefeber, T. van Terwisga, B. Cerup-Simonsen, and R. Folso. A systematic experimental study on powering performance of flapping foil propulsors. *29th Symposium on Naval Hydrodynamics*, August 26-31 2012. Gothenburg, Sweden.
- A. von Loebbecke, R. Mittal, F. Fish, and R. Mark. Propulsive efficiency of the underwater dolphin kick in humans. *J Biomech Eng.*, 131(5):054504, 2009.
- John Young, Simon M Walker, Richard J Bomphrey, Graham K Taylor, and Adrian LR Thomas. Details of insect wing design and deformation enhance aerodynamic function and flight efficiency. *Science*, 325(5947):1549–1552, 2009.
- Q. Zhu, M.J. Wolfgang, D.K.P. Yue, and M.S. Triantafyllou. Three-dimensional flow structures and vorticity control in fish-like swimming. *J. Fluid Mech.*, 468:1–28, 2002.



**RESEARCH CENTRE
BORDEAUX – SUD-OUEST**

200 avenue de la Vieille Tour
33405 Talence Cedex

Publisher
Inria
Domaine de Voluceau - Rocquencourt
BP 105 - 78153 Le Chesnay Cedex
inria.fr

ISSN 0249-6399